
PETRV2: A Unified Framework for 3D Perception from Multi-Camera Images

Yingfei Liu Junjie Yan Fan Jia Shuailin Li Qi Gao
 Tiancai Wang Xiangyu Zhang Jian Sun
 MEGVII Technology

Abstract

In this paper, we propose PETRV2, a unified framework for 3D perception from multi-view images. Based on PETR [21], PETRV2 explores the effectiveness of temporal modeling, which utilizes the temporal information of previous frames to boost 3D object detection. More specifically, we extend the 3D position embedding (3D PE) in PETR for temporal modeling. The 3D PE achieves the temporal alignment on object position of different frames. A feature-guided position encoder is further introduced to improve the data adaptability of 3D PE. To support for high-quality BEV segmentation, PETRV2 provides a simply yet effective solution by adding a set of segmentation queries. Each segmentation query is responsible for segmenting one specific patch of BEV map. PETRV2 achieves state-of-the-art performance on 3D object detection and BEV segmentation. Detailed robustness analysis is also conducted on PETR framework. We hope PETRV2 can serve as a unified framework for 3D perception.

1 Introduction

Recently, 3D perception from multi-camera images for autonomous driving system has drawn a great attention. The multi-camera 3D object detection methods can be divided into BEV-based [11, 10] and DETR-based [38, 21, 18] approaches. BEV-based methods (e.g., BEVDet [11]) explicitly transform the multi-view features into bird-eye-view (BEV) representation by LSS [30]. Different from the BEV-based counterparts, DETR-based approaches [38] models each 3D object as an object query and achieve end-to-end modeling with Hungarian algorithm [15]. Among these methods, PETR [21], based on DETR [3], converts the multi-view 2D features to 3D position-aware features by adding 3D position embedding (3D PE). The object query, initialized from 3D space, can directly perceive the 3D object information by interacting with the produced 3D position-aware features. In this paper, we aim to build a stronger and unified framework by extending PETR with temporal modeling and support for BEV segmentation.

For temporal modeling, the main problem is how to align the object position of different frames in 3D space. Existing works [10, 18] solved this problem from the perspective of feature alignment. For example, BEVDet4D [10] explicitly aligns the BEV feature of previous frame with current frame by pose transformation. However, PETR implicitly encodes the 3D position into the 2D image features and fails to perform the explicit feature transformation. Since PETR has demonstrated the effectiveness of 3D PE (encoding the 3D coordinates into 2D features) in 3D perception, we wonder if 3D PE still works on temporal alignment. In PETR, the meshgrid points of camera frustum space, shared for different views, are transformed to the 3D coordinates by camera parameters. The 3D coordinates are then input to a simple multi-layer perception (MLP) to generate the 3D PE. In our practice, we find that PETR works well under temporal condition by simply aligning the 3D coordinates of previous frame with the current frame.

For the joint learning with BEV segmentation, BEVFormer [18] provides a unified solution. It defines each point on BEV map as one BEV query. Thus, the BEV query can be employed for 3D object detection and BEV segmentation. However, the number of BEV query (e.g., $>60,000$) tends to be huge when the resolution of BEV map is relatively larger (e.g., 256×256). Such definition on object query is obviously not suitable for PETR due to the global attention employed in transformer decoder. In this paper, we design a simple and elegant solution for BEV segmentation. Inspired by the advanced instance segmentation methods [5, 32, 34, 6] where an instance mask within the bounding box is represented by a set of learnable parameters, we regard each patch of the BEV map as the mask within a bounding box and parameterize these BEV patches by different object queries. Despite object query for object detection (det query), we further introduce the so-called segmentation query (seg query) for BEV segmentation. The seg queries are initialized under BEV space and each seg query is responsible for segmenting specific patch. The updated seg queries from the transformer decoder are further used to predict the semantic map of corresponding patch. In this way, high-quality BEV segmentation can be achieved by simply adding a small number of (e.g., 256) seg queries.

Besides, we also improve the generation of 3D PE and provide a detailed robustness analysis on PETRv2. As mentioned above, the 3D PE is generated based on the fixed meshgrid points in camera frustum space. All images from one camera view share the 3D PE, making 3D PE data-independent. In this paper, we further improve the original 3D PE by introducing a feature-guided position encoder (FPE). Concretely, the projected 2D features are firstly injected into a small MLP network and a Sigmoid layer to generate the attention weight, which is used to reweight the 3D PE in an element-wise manner. The improved 3D PE is data-dependent, providing the informative guidance for the query learning in transformer decoder. For comprehensive robustness analysis on PETRv2, we consider multiple real noise cases including the camera extrinsics noise, camera miss and time delay.

To summarize, our contributions are:

- We study a conceptually simple extension of position embedding transformation to temporal representation learning. The temporal alignment can be achieved by the pose transformation on 3D PE. A feature-guided position encoder is further proposed to reweight the 3D PE with the guidance from 2D image features.
- A simple yet effective solution is introduced for PETR to support the joint learning of BEV segmentation. High-quality segmentation performance is achieved by simply adding small number of object queries.
- Experiments show that the proposed framework achieves state-of-the-art performance on both 3D object detection and BEV segmentation. Detailed robustness analysis is also provided for comprehensive evaluation on PETR framework.

2 Related Work

2.1 Multi-View 3D Object Detection

Previous works [4, 26, 13, 14, 33, 12, 1, 36, 35] perform 3D object detection mainly under the mono setting. Recently, 3D object detection based on multi-view images has attracted more attention. ImVoxelNet [31] and BEVDet [11] projected the multi-view image features into BEV representation. Then the 3D object detection can be performed using the methods from 3D point cloud, like [41]. DETR3D [38] and PETR [21] conduct the 3D object detection mainly inspired by the end-to-end DETR [3, 44, 25, 20]. The object queries are defined in 3D space and interact with the multi-view image features in transformer decoder. BEVFormer [18] further introduces the temporal information into vision-based 3D object detection. The spatial cross-attention is adopted to aggregate image features, while temporal self-attention is used to fuse the history BEV features. BEVDet4D [10] extends the BEVDet [11] by temporal modeling and achieves good speed estimation. Both BEVFormer [18] and BEVDet4D [10] align the multi-frame features in BEV space. Different from them, we extend the temporal version from PETR and achieve the temporal alignment from the perspective of 3D position embedding.

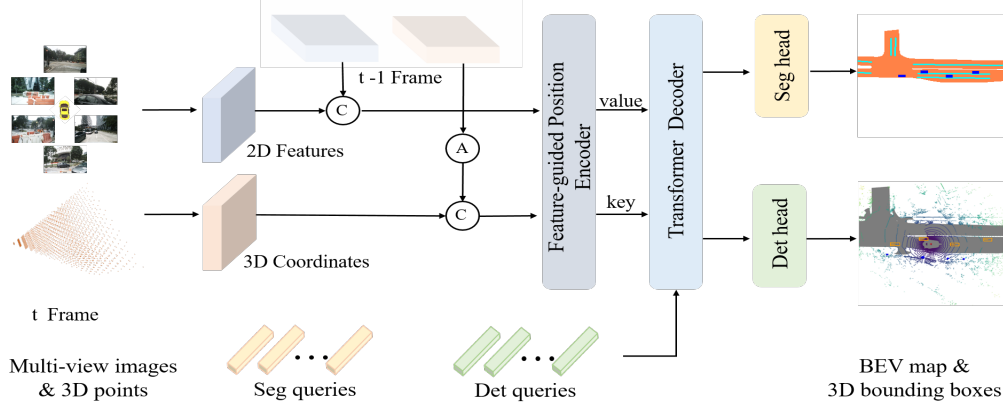


Figure 1: The paradigm of the proposed PETRv2. The 2D features are extracted by the backbone network from the multi-view images and the 3D coordinates are generated following the same way as PETR [21]. To achieve the temporal alignment, the 3D coordinates in PETR of previous frame $t - 1$ are firstly transformed through pose transformation. Then 2D image features and 3D coordinates of two frames are concatenated together and injected to feature-guided position encoder to generate the key and value components for the transformer decoder. The detection and segmentation queries, initialized by 3D anchor points and BEV points respectively, interact with the key and value components in transformer decoder. The updated queries are further used to predict the 3D bounding boxes and high-quality map with the detection and segmentation heads. \textcircled{A} is the 3D coordinates alignment from frame $t - 1$ to frame t . \textcircled{C} is concatenation operation along the batch axis.

2.2 BEV Segmentation

BEV segmentation focus on the perception in the BEV view. BEV segmentation takes the multi view images as input and rasterizes output onto a map view. VPN [27] proposes a view parsing network under the simulated environments and then transfers it to real-world environments to perform cross-view semantic segmentation. LSS [30] transforms the 2D features into 3D space by implicit estimation of depth and employs different heads for BEV segmentation and planning. M²BEV [39] further uses the camera parameters to project the features extracted from backbone to the 3D ego-car coordinate to generate the BEV representation. Then multi-task heads are used for 3D detection and segmentation. BEVFormer [18] generates the BEV features from multi-camera inputs by interacting the predefined grid-shaped BEV queries with the 2D image features. CVT [42] uses cross-view transformer to learn geometric transformation implicitly and directly from data. HDMapNet [17] transforms multi-view images to BEV view and produces a vectorized local semantic map. BEVsegformer [29] proposes multi-camera deformable attention to construct semantic map.

3 Method

3.1 Overall Architecture

As illustrated in Fig. 1, the overall architecture of PETRv2 is built upon the PETR [21] and extended with temporal modeling and BEV segmentation. The 2D image features are extracted from multi-view images with the 2D backbone (e.g., ResNet-50), and the 3D coordinates are generated from camera frustum space as described in PETR [21]. Considering the ego motion, 3D coordinates of the previous frame $t - 1$ are first transformed into the coordinate system of current frame t through the pose transformation. Then, the 2D features and 3D coordinates of adjacent frames are respectively concatenated together and input to the feature-guided position encoder (FPE). After that, the FPE is employed to generate the key and value components for the transformer decoder. Further, detection queries (det queries) and segmentation queries (seg queries), which are initialized from learnable 3D anchor points [37] and fixed BEV points respectively, are fed into the transformer decoder and interact with multi-view image features. Lastly, the updated queries are input to the detection and segmentation heads separately for final prediction.

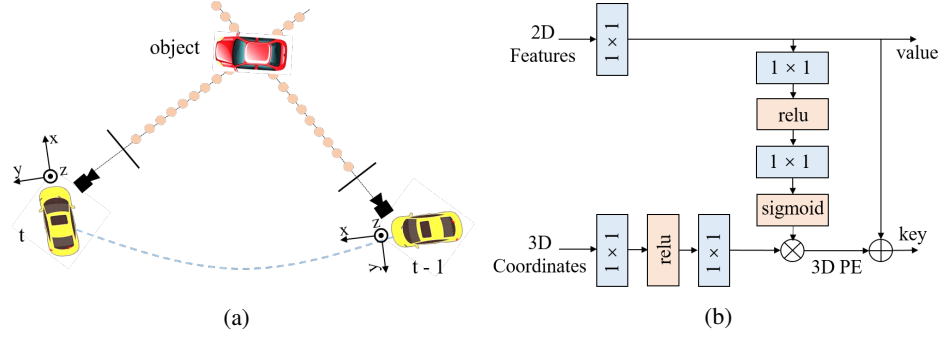


Figure 2: (a) The illustration of the coordinate system transformation from frame $t - 1$ to frame t . (b) Architecture of feature-guided position encoder. Different from PETR [21], 3D PE in PETRv2 is generated in a data-dependent way.

3.2 Temporal Modeling

PETR [21] leverages image features and projected 3D points to generate 3D features and works well in multi-view 3D detection. In this section, we extend it with the temporal modeling, which is realized by a 3D coordinates alignment (CA) and feature-guided position encoder (FPE), for better localization and speed estimation.

3D Coordinates Alignment The temporal alignment is to transform the 3D coordinates of frame $t - 1$ to the coordinate system of frame t (see Fig. 2(a)). For clarity, we first denote some coordinate systems: camera coordinate as $c(t)$, lidar coordinate as $l(t)$, and ego coordinate as $e(t)$ at frame t . What’s more, global coordinates as g . We define T_{src}^{dst} as the transformation matrix from the source coordinate system to the target coordinate system.

We use $l(t)$ as the default 3D space for multi-view camera 3D position-aware feature generation. The 3D points $P_i^{l(t)}(t)$ projected from i -th camera can be formulated as:

$$P_i^{l(t)}(t) = T_{c_i(t)}^{l(t)} K_i^{-1} P^m(t) \quad (1)$$

where $P^m(t)$ is the points set in the meshgrid of camera frustum space at frame t . $K_i \in R^{4 \times 4}$ is the camera intrinsic matrix of the i -th camera. Given the auxiliary frame $t - 1$, we align the coordinates of 3D points from frame $t - 1$ to frame t :

$$P_i^{l(t)}(t-1) = T_{l(t-1)}^{l(t)} P_i^{l(t-1)}(t-1) \quad (2)$$

With *global* coordinate space acting as a bridge between frame $t - 1$ and frame t , $T_{l(t-1)}^{l(t)}$ can be easily calculated:

$$T_{l(t-1)}^{l(t)} = T_{e(t)}^{l(t)} T_g^{e(t)} T_g^{e(t-1)-1} T_{e(t-1)}^{l(t-1)-1} \quad (3)$$

The aligned point sets $[P_i^{l(t)}(t-1), P_i^{l(t)}(t)]$ will be used to generate the 3D position embedding, as described below.

Feature-guided Position Encoder PETR [21] transforms the 3D coordinates into 3D position embedding (3D PE). The generation of 3D position embedding can be formulated as:

$$PE_i^{3d}(t) = \psi(P_i^{l(t)}(t)) \quad (4)$$

where $\psi(\cdot)$ is a simple multi-layer perception (MLP). The 3D PE in PETR is independent with the input image. We argue that the 3D PE should be driven by the 2D features since the image feature can provide some informative guidance (e.g., depth). In this paper, we propose a feature-guided position encoder, which implicitly introduces vision prior. The generation of feature-guided 3D position embedding can be formulated as:

$$PE_i^{3d}(t) = \xi(F_i(t)) * \psi(P_i^{l(t)}(t)) \quad (5)$$

where ξ is also a small MLP network. $F_i(t)$ is the 2D image features of the i -th camera. As illustrated in Fig. 2(b), the 2D image features projected by a 1×1 convolution are fed into a small MLP network

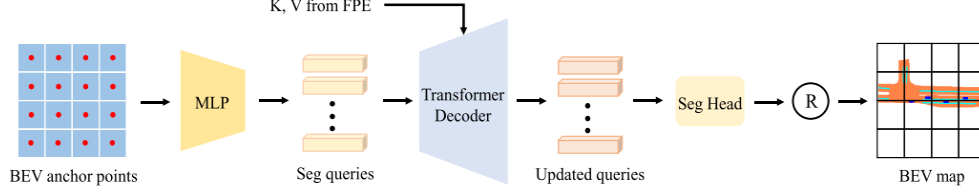


Figure 3: The architecture of BEV segmentation branch. The seg queries, uniformly initialized by the anchor points in BEV space, update the representation by transformer decoder. The updated queries are further input to the segmentation head to predict the BEV map. \textcircled{R} is the reshape operation.

ξ and Sigmoid function to obtain the attention weights. The 3D coordinates are transformed by another MLP network ψ and multiplied with the attention weights to generate the 3D PE. The 3D PE is added with 2D features to obtain the key value for transformer decoder. The projected 2D features are used as the value component for transformer decoder.

3.3 BEV Segmentation

In this section, we aim to equip the PETR [21] with seg queries to support high-quality BEV segmentation. A high-resolution BEV map can be partitioned into a small number of patches. We introduce the seg query for BEV segmentation and each seg query corresponds to a specific patch (e.g., top-left 16×16 pixels of the BEV map). As shown in Fig. 3, the seg queries are initialized with fixed anchor points in BEV space, similar to the generation of detection query (det query) in PETR. These anchor points are then projected into the seg queries by a simple MLP with two linear layers. After that, the seg queries are input to the transformer decoder and interact with the image features. For the transformer decoder, we use the same framework as detection task. Then the updated seg queries are finally fed into the segmentation head (a simple MLP network followed by a Sigmoid layer) to predict the BEV embeddings. Each BEV embedding is reshaped to a BEV patch (of shape 16×16). All BEV patches are concatenated together in spatial dimension to produce the segmentation results (of shape 256×256). For segmentation branch, the weighted cross-entropy loss is employed for supervision on the predicted BEV map:

$$\ell_{seg} = \frac{1}{N} \sum_{j=0}^C \sum_{i=0}^N \omega \hat{y}_i \log(y_i) + (1 - \hat{y}_i) \log(1 - y_i) \quad (6)$$

where N is the number of pixels in ground truth, C is the number of object categories. \hat{y} is the segmentation label and y is the predicted BEV map. ω is the weight of positive samples and calculated by the proportion between the negative samples and the positive samples in ground truth.

3.4 Robust Analysis

Though recently there are lots of works on autonomous driving systems, only a few [30, 18] explore the robustness of proposed methods. LSS [30] presents the performance under extrinsics noises and camera dropout at test time. Similarly, BEVFormer [18] demonstrates the robustness of model variants to camera extrinsics. In practice, there are diverse sensor errors and system biases, and it is important to validate the effect of these circumstances due to the high requirements of safety and reliability. We aim to give an extensive study of our method under different conditions.

As shown in Fig. 4, we focus on three common types of sensor errors as follows:

Extrinsics noise: Extrinsics noises are common in reality, such as camera shake caused by a car bump or camera offset by environmental forces. In these cases, extrinsics provided by the system is inaccurate and the perceptual output will be affected.

Camera miss: Camera image miss occurs when one camera breaks down or is occluded. Multiview images provide panoramic visual information, yet the possibility exists that one of them is absent in the real world. It is necessary to evaluate the importance of these images so as to prepare the strategy of sensor redundancy in advance.

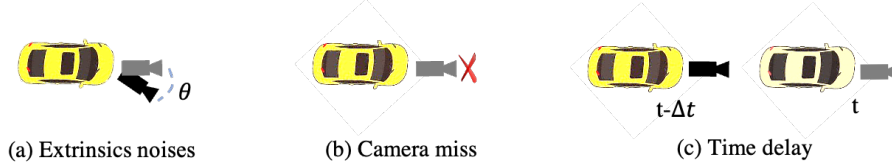


Figure 4: We investigate the system robustness under three typical sensor errors.

Camera time delay: Camera time delay is also a challenge due to the camera exposure time, especially in night. The long exposure time causes the system is fed with images from the previous time, and brings the significant output offsets.

4 Experiments

4.1 Datasets and Metrics

We evaluate our approach on nuScenes benchmark [2]. NuScenes [2] is a large-scale multimodal dataset that is composed of data collected from 6 cameras, 1 lidar and 5 radars. The dataset has 1000 scenes and is officially divided into 700/150/150 scenes for training/validation/testing, respectively. We mainly focus on two sub-tasks: 3D object detection and BEV segmentation.

For 3D object detection, each scene has 20s video frames and is fully annotated with 3D bounding boxes every 0.5s. Consistent with official evaluation metrics, we report nuScenes Detection Score (NDS), mean Average Precision (mAP), and five True Positive (TP) metrics: mean Average Translation Error (mATE), mean Average Scale Error (mASE), mean Average Orientation Error (mAOE), mean Average Velocity Error (mAVE), mean Average Attribute Error (mAAE). NDS is a comprehensive indicator to evaluate the detection performance.

For BEV segmentation, we follow LSS [30] and use IoU score as the metric. The ground-truth includes three different categories: Driveable area, Lane and Vehicle. The lane category is formed by two map layers: lane-Divider and Road-Divider. For Vehicle segmentation, we obtain the BEV ground truth by projecting 3D bounding boxes into the BEV plane [30]. The Vehicle segmentation ground truth refers to all bounding boxes of meta-category Vehicle, which contains bicycle, bus, car, construction, motorcycle, trailer and truck.

4.2 Implementation Details

In our implementation, ResNet [8] and VoVNetV2 [16] are employed as the backbone network. The P4 feature (merging the C4 and C5 features from backbone) with 1/16 input resolution is used as the 2D feature. The generation of 3D coordinates is consistent with PETR [21]. Following BEVDet4D [10], we randomly sample a frame as previous frame from $[3T; 27T]$ during training, and sample the frame at $15T$ during inference. $T (\approx 0.083)$ is the time interval between two sweep frames. Our model is trained using AdamW [24] optimizer with a weight decay of 0.01. The learning rate is initialized with 2.0×10^{-4} and decayed with cosine annealing policy [23]. All experiments are trained for 24 epochs (2x schedule) on 8 Tesla A100 GPUs with a batch size of 8 except for the ablations. No test time augmentation methods are used during inference.

For 3D object detection, we perform experiments with 1500 det queries on nuScenes test dataset. Following the settings in PETR [21], we initialize a set of learnable anchor points in 3D world space, and generate these queries through a small MLP network. Similar to FCOS3D [36], we add extra disentangled layers for regression targets. We also adopt the focal loss [19] for classification and $L1$ loss for 3D bounding box regression. The Hungarian algorithm [15] is used for label assignment between ground-truths and predictions.

For BEV segmentation, we follow the settings in [30]. We use the map layers provided by the nuScenes dataset to generate the 256×256 BEV map ground truth. We set the patch size to 16×16 and 256 seg queries are used to predict the final BEV segmentation result.

Table 1: Comparison of recent works on the nuScenes test set. * are trained with external data. ‡ is test time augmentation.

Methods	Backbone	NDS↑	mAP↑	mATE↓	mASE↓	mAOE↓	mAVE↓	mAAE↓
CenterNet [43]	DLA	0.400	0.338	0.658	0.255	0.629	1.629	0.142
FCOS3D‡ [36]	Res-101	0.428	0.358	0.690	0.249	0.452	1.434	0.124
PGD‡ [35]	Res-101	0.448	0.386	0.626	0.245	0.451	1.509	0.127
DD3D*‡ [28]	V2-99	0.477	0.418	0.572	0.249	0.368	1.014	0.124
DETR3D* [38]	V2-99	0.479	0.412	0.641	0.255	0.394	0.845	0.133
BEVDet [11]	Swin-S	0.463	0.398	0.556	0.239	0.414	1.010	0.153
BEVDet* [11]	V2-99	0.488	0.424	0.524	0.242	0.373	0.950	0.148
M ² BEV [39]	X-101	0.474	0.429	0.583	0.254	0.376	1.053	0.190
PETR* [21]	V2-99	0.504	0.441	0.593	0.249	0.383	0.808	0.132
BEVFormer* [18]	V2-99	0.569	0.481	0.582	0.256	0.375	0.378	0.126
BEVDet4D [10]	Swin-B	0.569	0.451	0.511	0.241	0.386	0.301	0.121
PETRv2*	V2-99	0.582	0.490	0.561	0.243	0.361	0.343	0.120

Table 2: Comparison of recent BEV segmentation works on the nuScenes val set. * are trained with external data. The performance of M²BEV is reported with X-101 [40] backbone.

Methods	Backbone	IoU-Drive↑	IoU-Lane↑	IoU-Vehicle↑
Lift-Splat [30]	Res-101	0.729	0.200	0.321
FIERY [9]	Res-101	-	-	0.382
M ² BEV [39]	X-101	0.759	0.380	-
BEVFormer [18]	Res-101	0.775	0.239	0.467
PETRv2	Res-101	0.783	0.430	0.485
PETRv2*	V2-99	0.799	0.459	0.517

To simulate extrinsic noises and evaluate the effect, we choose to randomly apply 3D rotation to camera extrinsics. 3D rotation is very common and typical in real scenarios, and we ignore other noisy patterns such as translation to avoid multi-variable interference. Specifically, we randomly choose one from multiple cameras to apply 3D rotation. Denoting α, β, γ as angles (in degree) along X, Y, Z axes respectively, we investigate in several rotation settings with maximum amplitudes $\alpha_{max}, \beta_{max}, \gamma_{max} \in \{2, 4, 6, 8\}$, where $\alpha_{max} = 2$ means that α is uniformly sampled from $[-2, 2]$, for example. In experiment, we use $R_{max} = M$ to denote $\alpha_{max} = \beta_{max} = \gamma_{max} = M$.

4.3 State-of-the-art Comparison

Tab. 1 shows the performance comparison of 3D detection on nuScenes test set. Our method achieves state-of-the-art performance among public methods. Our PETRv2 with VoVNet surpasses the PETR by a large margin (7.8% NDS and 4.9% mAP). Benefiting from the temporal modeling, the mAVE is achieved with 0.343m/s compared to the 0.808m/s of PETR. When compared with other temporal methods, PETRv2 surpasses the BEVDet4D [10] with Swin-Base [22] and BEVFormer [18] V2-99 [16] by 1.3% NDS. It shows that the temporal alignment by 3D PE can also achieve remarkable performance. It should be noted that PETRv2 can be easily employed for practical application without the explicit feature alignment.

We also compare the BEV segmentation performance on nuScenes dataset. As shown in Tab. 2, we conduct the experiments with ResNet-101 and VoV-99 backbones. Since PETRv2 is the temporal extension of PETR so we mainly compare the performance with BEVFormer for fair comparison. With ResNet-101 backbone, our PETRv2 outperforms BEVFormer on IoU-lane metric and IoU-Vehicle by a large margin and achieves comparable performances on the IoU-drive metrics. With the stronger pretrained VoV-99 backbone, our PETRv2 achieves state-of-the-art performance. It shows that the joint learning of detection and segmentation branches will introduce the performance drop for segmentation branches. This may owe to the representation gap between these two tasks, especially for the drive and lane region. For qualitative results, please refer to the visualizations in A.1.

Table 3: The ablation studies of different components in the proposed PETRv2. PETRv2 uses two frame images as input by default.

	CA	FPE	NDS \uparrow	mAP \uparrow	mATE \downarrow	mASE \downarrow	mAOE \downarrow	mAVE \downarrow	mAAE \downarrow
PETR			0.434	0.379	0.754	0.272	0.476	0.838	0.211
PETR		✓	0.449	0.381	0.749	0.271	0.462	0.736	0.200
PETRv2			0.461	0.384	0.775	0.270	0.470	0.605	0.189
PETRv2	✓		0.482	0.393	0.774	0.272	0.486	0.429	0.187
PETRv2	✓	✓	0.496	0.401	0.745	0.268	0.448	0.394	0.184

(a) The impact of 3D coordinates alignment and feature-guided Position Encoder. CA is the 3D coordinates alignment. FPE is the proposed feature-guided position encoder.

Queries	Patch size	Drive	Lane	Vehicle
256	16×16	0.791	0.443	0.494
64	32×32	0.773	0.414	0.425
128	32×16	0.778	0.425	0.441
128	16×32	0.777	0.410	0.455
256	32×32	0.788	0.441	0.496

(b) Result of different patch size on the nuScenes val set. The patch size gradually increases from 16×16 to 32×32 .

Det	Seg	NDS	mAP	Drive	Lane	Vehicle
0.0	1.0	-	-	0.805	0.474	0.508
1.0	0.0	0.496	0.401	-	-	-
1.0	0.5	0.492	0.398	0.783	0.426	0.489
1.0	1.0	0.495	0.401	0.791	0.443	0.494
1.0	2.0	0.487	0.396	0.803	0.473	0.509

(c) Result of different loss weight on the nuScenes val set. We explore the effect of joint training by modifying the weights of the two branches.

4.4 Ablation Study

In this section, we conduct the ablations with VoVNet-99 backbone. The backbone is pretrained on DDAM15M dataset [28] and train set of Nuscenes [2]. The input image size is of size 800×320 and the model is trained with 24 epochs. The number of detection queries is set to 900.

Temporal Modeling. Here we first explore the effect of two components in temporal modeling: 3D coordinates alignment (CA) and feature-guided position encoder (FPE). For this ablation, we only trained the detection branch for clarity. As shown in Tab. 3(a), without CA, PETRv2 only improves the performance by 2.7% NDS and 0.5% mAP. With CA, the performance is further improved by 2.1% NDS and 0.9% mAP. The mAVE metric is 0.429 m/s, which shows a large margin compared to the PETR baseline. To verify the effectiveness of FPE, we replace the 3D position encoder in PETR with FPE. The NDS metric is increased by 1.5% while mAP is only increased by 0.2%. When applied the FPE on PETRv2, the mAP achieves a relatively higher improvement (0.8%). It indicates that FPE module is also beneficial for the temporal version.

Segmentation Query. We further explore the effect of the seg query number and the patch size that each query is assigned (see Tab. 3(b)). The loss weight of segmentation branch is set to 1. In order to keep the size of the predicted BEV map unchanged, the number of queries is correspondingly reduced to 1/4 when the patch size is doubled. Experimental results show that the best performance is achieved when the query number is set to 256 and the patch size is set to 32×32 .

Analysis on Multi-task Learning. We also perform the analysis on the effect of multi-task learning (see Tab. 3(c)). It can be observed that 3D detection and BEV segmentation tasks do not promote each other. When the weights of the detection and segmentation branches are the same (1.0), the performance of BEV segmentation on IoU-lane metric decreases by 3.1% compared to the baseline (segmentation only). Recently, some other studies [7, 39] also pointed out that not all the 3D computer vision tasks can benefit from other tasks in the joint training setting. While in our practice, good trade-off performance can be achieved when the weight of segmentation branch is set to 2.

4.5 Robustness analysis

Tab. 4 reports a summary of quantitative results on nuScenes dataset with extrinsics noises. We compare PETRv2, PETR and PETR + FPE (FPE denotes the Feature-guided Position Encoder). As the noise increases, the performance of all three models decreases continually, indicating the impact of extrinsics noises. In the extreme noise setting $R_{max} = 8$, PETRv2 drops 4.12% mAP and 2.85% NDS, PETR+FPE drops 4.68% mAP and 3.42% NDS, while PETR drops 6.33% mAP and 4.54%

Table 4: Quantitative results on the nuScenes val set with extrinsics noises. The metrics in each cell are mAP(NDS)[%]. $R_{max} = M$ denotes the maximum angle of three axes is M in degree.

Methods	Original val	$R_{max} = 2$	$R_{max} = 4$	$R_{max} = 6$	$R_{max} = 8$
PETrv2	40.08 (49.63)	39.13 (48.98)	37.69 (47.93)	36.66 (47.24)	35.96 (46.78)
PETR	38.13 (44.88)	37.17 (44.16)	35.83 (43.10)	34.47 (42.17)	33.45 (41.46)
PETR+FPE	37.87 (43.37)	36.71 (42.50)	34.58 (40.88)	32.79 (39.61)	31.54 (38.83)

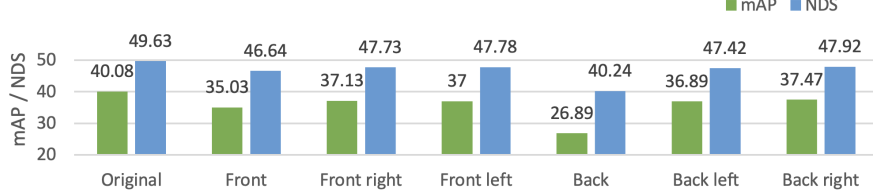


Figure 5: The performance on nuScenes val when losing each of camera images.

NDS. We observe that FPE improves the robustness to extrinsics noises, while temporal extension with multiple frames does not bring significant robustness gains.

We also show how the model performs when randomly losing one camera in Fig. 5. Among six cameras of nuScenes dataset, Front and Back cameras are the most important, and their absence leads to a drop of 5.05% and 13.19% mAP respectively. The Back camera is especially essential due to its large field of view (180°). Losing other cameras also brings an average performance decrease of 2.93% mAP and 1.93% NDS. Note that the overlap region between cameras is small for nuScenes, thus any camera miss is hard to compensate by adjacent ones. In practice, sensor redundancy is necessary in case of emergency, and the complementary of cameras requires deeper explorations.

The effect of camera time delay is demonstrated in Tab. 5. In nuScenes, keyframes are attached with groundtruth annotations, and we leverage unannotated frames between key frames as input images to simulate the time delay. The delay of 0.083s leads to a drop of 3.19% mAP and 8.4% NDS, indicating the significant impact of time delay. When time delay increase to over 0.3s, the performance sharply decreases to 26.08% mAP and 36.54% NDS. Since time delay is inevitable in real-world systems and affects detection a lot, more attention is supposed to pay to it.

Table 5: The performance impact of camera time delay. Time delay unit $T \approx 0.083$ s.

Time delay	Original	T	2T	3T	4T
PETrv2	40.08 (49.63)	36.89 (41.23)	33.99 (39.00)	30.91 (36.88)	26.08 (36.54)

5 Conclusion

In this paper, we introduce the PETrv2, a unified framework for 3D perception from multi-camera images. PETrv2 extends the PETR baseline with temporal modeling and multi-task learning. With the temporal alignment on 3D position embedding, PETrv2 naturally achieves the multi-frame modeling and improves the 3D detection performance. PETrv2 also supports the multi-task learning, such as BEV segmentation, by adding a set of task-related queries. For a fully understanding of PETrv2 framework, we further provide a detailed analysis on the robustness of PETrv2 under three types of sensor errors. We hope PETrv2 can serve as a strong baseline and a unified framework for 3D perception. In the near future, we will explore more vision tasks (e.g., 3D lane detection) and multi-modal fusion for autonomous driving system.

References

- [1] Garrick Brazil and Xiaoming Liu. M3d-rpn: Monocular 3d region proposal network for object detection. In *Proceedings of the IEEE/CVF International Conference on Computer Vision*, pages 9287–9296, 2019.
- [2] Holger Caesar, Varun Bankiti, Alex H Lang, Sourabh Vora, Venice Erin Liong, Qiang Xu, Anush Krishnan, Yu Pan, Giancarlo Baldan, and Oscar Beijbom. nuscenes: A multimodal dataset for autonomous driving. In *Proceedings of the IEEE/CVF conference on computer vision and pattern recognition*, pages 11621–11631, 2020.
- [3] Nicolas Carion, Francisco Massa, Gabriel Synnaeve, Nicolas Usunier, Alexander Kirillov, and Sergey Zagoruyko. End-to-end object detection with transformers. In *European conference on computer vision*, pages 213–229. Springer, 2020.
- [4] Xiaozhi Chen, Kaustav Kundu, Ziyu Zhang, Huimin Ma, Sanja Fidler, and Raquel Urtasun. Monocular 3d object detection for autonomous driving. In *Proceedings of the IEEE conference on computer vision and pattern recognition*, pages 2147–2156, 2016.
- [5] Bin Dong, Fangao Zeng, Tiancai Wang, Xiangyu Zhang, and Yichen Wei. Solq: Segmenting objects by learning queries. *Advances in Neural Information Processing Systems*, 34, 2021.
- [6] Yuxin Fang, Shusheng Yang, Xinggang Wang, Yu Li, Chen Fang, Ying Shan, Bin Feng, and Wenyu Liu. Instances as queries. *Proc. IEEE Conf. Comp. Vis. Patt. Recogn.*, 2021.
- [7] Chris Fifty, Ehsan Amid, Zhe Zhao, Tianhe Yu, Rohan Anil, and Chelsea Finn. Efficiently identifying task groupings for multi-task learning. *Advances in Neural Information Processing Systems*, 34, 2021.
- [8] Kaiming He, Xiangyu Zhang, Shaoqing Ren, and Jian Sun. Deep residual learning for image recognition. In *Proceedings of the IEEE conference on computer vision and pattern recognition*, pages 770–778, 2016.
- [9] Anthony Hu, Zak Murez, Nikhil Mohan, Sofia Dudas, Jeffrey Hawke, Vijay Badrinarayanan, Roberto Cipolla, and Alex Kendall. Fiery: Future instance prediction in bird’s-eye view from surround monocular cameras. In *Proceedings of the IEEE/CVF International Conference on Computer Vision*, pages 15273–15282, 2021.
- [10] Junjie Huang and Guan Huang. Bevdet4d: Exploit temporal cues in multi-camera 3d object detection. *arXiv preprint arXiv:2203.17054*, 2021.
- [11] Junjie Huang, Guan Huang, Zheng Zhu, and Dalong Du. Bevdet: High-performance multi-camera 3d object detection in bird-eye-view. *arXiv preprint arXiv:2112.11790*, 2021.
- [12] Eskil Jørgensen, Christopher Zach, and Fredrik Kahl. Monocular 3d object detection and box fitting trained end-to-end using intersection-over-union loss. *arXiv preprint arXiv:1906.08070*, 2019.
- [13] Wadim Kehl, Fabian Manhardt, Federico Tombari, Slobodan Ilic, and Nassir Navab. Ssd-6d: Making rgb-based 3d detection and 6d pose estimation great again. In *Proceedings of the IEEE international conference on computer vision*, pages 1521–1529, 2017.
- [14] Jason Ku, Alex D Pon, and Steven L Waslander. Monocular 3d object detection leveraging accurate proposals and shape reconstruction. In *Proceedings of the IEEE/CVF conference on computer vision and pattern recognition*, pages 11867–11876, 2019.
- [15] Harold W Kuhn. The hungarian method for the assignment problem. *Naval research logistics quarterly*, 2(1-2):83–97, 1955.
- [16] Youngwan Lee and Jongyoul Park. Centermask: Real-time anchor-free instance segmentation. In *Proceedings of the IEEE/CVF conference on computer vision and pattern recognition*, pages 13906–13915, 2020.
- [17] Qi Li, Yue Wang, Yilun Wang, and Hang Zhao. Hdmapnet: A local semantic map learning and evaluation framework. *arXiv preprint arXiv:2107.06307*, 2021.
- [18] Zhiqi Li, Wenhai Wang, Hongyang Li, Enze Xie, Chonghao Sima, Tong Lu, Qiao Yu, and Jifeng Dai. Bevformer: Learning bird’s-eye-view representation from multi-camera images via spatiotemporal transformers. *arXiv preprint arXiv:2203.17270*, 2022.

- [19] Tsung-Yi Lin, Priya Goyal, Ross Girshick, Kaiming He, and Piotr Dollár. Focal loss for dense object detection. In *Proceedings of the IEEE international conference on computer vision*, pages 2980–2988, 2017.
- [20] Shilong Liu, Feng Li, Hao Zhang, Xiao Yang, Xianbiao Qi, Hang Su, Jun Zhu, and Lei Zhang. Dab-detr: Dynamic anchor boxes are better queries for detr. *arXiv preprint arXiv:2201.12329*, 2022.
- [21] Yingfei Liu, Tiancai Wang, Xiangyu Zhang, and Jian Sun. Petr: Position embedding transformation for multi-view 3d object detection. *arXiv preprint arXiv:2203.05625*, 2022.
- [22] Ze Liu, Yutong Lin, Yue Cao, Han Hu, Yixuan Wei, Zheng Zhang, Stephen Lin, and Baining Guo. Swin transformer: Hierarchical vision transformer using shifted windows. In *Proceedings of the IEEE/CVF International Conference on Computer Vision*, pages 10012–10022, 2021.
- [23] Ilya Loshchilov and Frank Hutter. Sgdr: Stochastic gradient descent with warm restarts. *arXiv preprint arXiv:1608.03983*, 2016.
- [24] Ilya Loshchilov and Frank Hutter. Decoupled weight decay regularization. *arXiv preprint arXiv:1711.05101*, 2017.
- [25] Depu Meng, Xiaokang Chen, Zejie Fan, Gang Zeng, Houqiang Li, Yuhui Yuan, Lei Sun, and Jingdong Wang. Conditional detr for fast training convergence. In *Proceedings of the IEEE/CVF International Conference on Computer Vision*, pages 3651–3660, 2021.
- [26] Arsalan Mousavian, Dragomir Anguelov, John Flynn, and Jana Kosecka. 3d bounding box estimation using deep learning and geometry. In *Proceedings of the IEEE conference on Computer Vision and Pattern Recognition*, pages 7074–7082, 2017.
- [27] Bowen Pan, Jiankai Sun, Ho Yin Tiga Leung, Alex Andonian, and Bolei Zhou. Cross-view semantic segmentation for sensing surroundings. *IEEE Robotics and Automation Letters*, 5(3):4867–4873, 2020.
- [28] Dennis Park, Rares Ambrus, Vitor Guizilini, Jie Li, and Adrien Gaidon. Is pseudo-lidar needed for monocular 3d object detection? In *Proceedings of the IEEE/CVF International Conference on Computer Vision*, pages 3142–3152, 2021.
- [29] Lang Peng, Zhirong Chen, Zhangjie Fu, Pengpeng Liang, and Erkang Cheng. Bevsegformer: Bird’s eye view semantic segmentation from arbitrary camera rigs. *arXiv preprint arXiv:2203.04050*, 2022.
- [30] Jonah Philion and Sanja Fidler. Lift, splat, shoot: Encoding images from arbitrary camera rigs by implicitly unprojecting to 3d. In *European Conference on Computer Vision*, pages 194–210. Springer, 2020.
- [31] Danila Rukhovich, Anna Vorontsova, and Anton Konushin. Imvoxelnet: Image to voxels projection for monocular and multi-view general-purpose 3d object detection. In *Proceedings of the IEEE/CVF Winter Conference on Applications of Computer Vision*, pages 2397–2406, 2022.
- [32] Xing Shen, Jirui Yang, Chunbo Wei, Bing Deng, Jianqiang Huang, Xiansheng Hua, Xiaoliang Cheng, and Kewei Liang. Dct-mask: Discrete cosine transform mask representation for instance segmentation. *arXiv:2011.09876*, 2020.
- [33] Andrea Simonelli, Samuel Rota Buló, Lorenzo Porzi, Manuel López-Antequera, and Peter Kotschieder. Disentangling monocular 3d object detection. In *Proceedings of the IEEE/CVF International Conference on Computer Vision*, pages 1991–1999, 2019.
- [34] Zhi Tian, Chunhua Shen, and Hao Chen. Conditional convolutions for instance segmentation. *Proc. Eur. Conf. Comp. Vis.*, 2020.
- [35] Tai Wang, ZHU Xinge, Jiangmiao Pang, and Dahua Lin. Probabilistic and geometric depth: Detecting objects in perspective. In *Conference on Robot Learning*, pages 1475–1485. PMLR, 2022.
- [36] Tai Wang, Xinge Zhu, Jiangmiao Pang, and Dahua Lin. Fcos3d: Fully convolutional one-stage monocular 3d object detection. In *Proceedings of the IEEE/CVF International Conference on Computer Vision*, pages 913–922, 2021.
- [37] Yingming Wang, Xiangyu Zhang, Tong Yang, and Jian Sun. Anchor detr: Query design for transformer-based detector. *arXiv preprint arXiv:2109.07107*, 2021.

- [38] Yue Wang, Guizilini Vitor Campagnolo, Tianyuan Zhang, Hang Zhao, and Justin Solomon. Detr3d: 3d object detection from multi-view images via 3d-to-2d queries. In *In Conference on Robot Learning*, pages 180–191, 2022.
- [39] Enze Xie, Zhiding Yu, Daquan Zhou, Jonah Philion, Anima Anandkumar, Sanja Fidler, Ping Luo, and Jose M Alvarez. M² 2bev: Multi-camera joint 3d detection and segmentation with unified birds-eye view representation. *arXiv preprint arXiv:2204.05088*, 2022.
- [40] Saining Xie, Ross Girshick, Piotr Dollár, Zhuowen Tu, and Kaiming He. Aggregated residual transformations for deep neural networks. In *Proceedings of the IEEE conference on computer vision and pattern recognition*, pages 1492–1500, 2017.
- [41] Tianwei Yin, Xingyi Zhou, and Philipp Krahenbuhl. Center-based 3d object detection and tracking. In *Proceedings of the IEEE/CVF conference on computer vision and pattern recognition*, pages 11784–11793, 2021.
- [42] Brady Zhou and Philipp Krähenbühl. Cross-view transformers for real-time map-view semantic segmentation. *arXiv preprint arXiv:2205.02833*, 2022.
- [43] Xingyi Zhou, Dequan Wang, and Philipp Krähenbühl. Objects as points. *arXiv preprint arXiv:1904.07850*, 2019.
- [44] Xizhou Zhu, Weijie Su, Lewei Lu, Bin Li, Xiaogang Wang, and Jifeng Dai. Deformable detr: Deformable transformers for end-to-end object detection. *arXiv preprint arXiv:2010.04159*, 2020.

A Appendix

A.1 Qualitative Results

We show some qualitative results in Fig. 6. Our method achieves good 3D detection and BEV segmentation performance under different conditions.

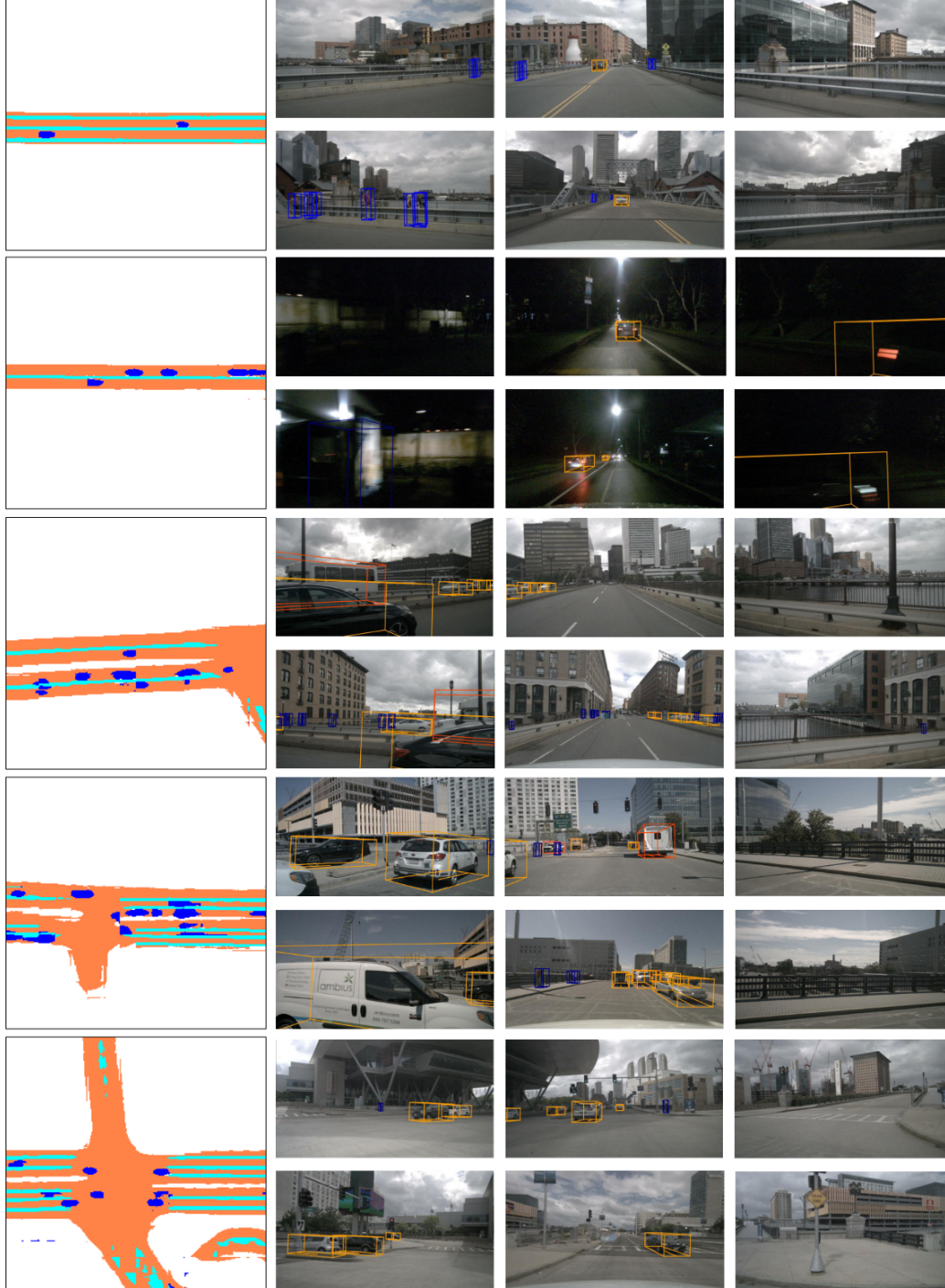


Figure 6: Qualitative results for 3D object detection and BEV segmentation.